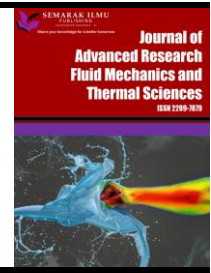




Journal of Advanced Research in Fluid Mechanics and Thermal Sciences

Journal homepage:
https://semarakilmu.com.my/journals/index.php/fluid_mechanics_thermal_sciences/index
ISSN: 2289-7879



Effect of the Turbulence Model on the Computational Results of a Lucid Spherical Rotor

Mabrouk Mosbahi^{1,4,*}, Mariem Lajnef², Mouna Derbel³, Zied Driss², Emanuele Amato^{4,5}, Calogero Picone⁴, Marco Sinagra⁵, Tullio Tucciarelli^{4,5}

¹ University of Tunis, Higher National Engineering School of Tunis (ENSIT), Avenue Taha Hussein Montfleury, 1008 Tunisia

² University of Sfax, Laboratory of Electro-Mechanic Systems, National School of Engineers of Sfax, B.P. 1173, km 3.5 Soukra, 3038 Sfax, Tunisia

³ CRMN, Centre for Research on Microelectronics and Nanotechnology of Sousse, MACSI, Code Postal 4054, Sousse, Tunisia

⁴ University of Palermo, Department of Engineering, 90128 Palermo, Italy

⁵ Sustainable Mobility Center (Centro Nazionale per la Mobilità Sostenibile—CNMS), Italy

ARTICLE INFO

ABSTRACT

Article history:

Received 13 August 2023

Received in revised form 10 December 2023

Accepted 21 December 2023

Available online 15 January 2024

Keywords:

Numerical simulations; URANS; turbulence models; Lucid spherical rotor

Due to the excessive increase in the energy demand, renewable energy has become an alternative for electricity production for industrial and domestic needs. Water energy has received significant investment as a sustainable and clean energy source. Lucid spherical rotors, a kind of hydro-power converter, are cross flow rotors designed to be mounted within a pipeline in order to gather excess energy available in gravity-fed water pipelines. This paper focuses on the effect of the numerical model parameters choice, namely the turbulence model, on the Lucid spherical rotor hydrodynamic characteristics. Numerical simulations were carried out through Ansys Fluent software 17.0 using the unsteady Reynolds-Averaged Navier-Stokes (URANS) equations. Four turbulence models: RNG k- ϵ , Realizable k- ϵ , SST k- ω and transition SST were tested. Performance characteristics in terms of torque and power coefficients in addition to hydrodynamic features of the flow around the considered rotor were analyzed. The adopted numerical model was validated based on previous experimental findings from the literature. It was found that the realizable k- ϵ model showed a good agreement with experimental results. Thus, it was adopted for the Lucid spherical rotor simulation. The obtained findings could provide further direction for researchers to use the Lucid spherical water turbine.

1. Introduction

Nowadays, energy is the most important need for human. It is considered to be a needed component in the development of country. It is essential in every activity of daily life including access to basic necessities, health and education [1,2]. Many methods are available to produce energy for humanity on the Earth. Fossil fuels are the most used energy sources since they are characterized by an easy exploit and an effective cost. However, the burning of these fuels

* Corresponding author.

E-mail address: mabrouk.mosbahi@gmail.com

<https://doi.org/10.37934/arfmts.113.1.2443>

increases the concentration of greenhouse gases such as carbon dioxide in the atmosphere. Indeed, the reserves of fossil fuels are started to decrease. To reduce greenhouse gas emissions and to provide sustainable energy services, renewable energy sources are increasingly recommended and used to produce green power [3,4]. Among all renewable energies, small-scale hydropower is considered to be the most cost-effective source and it has experienced a rapid growth globally [5]. In order to generate electricity from hydropower, a water rotor converts the kinetic energy from the water current to electrical power. There are basically two types of water rotors; the axial-flow rotors and the cross flow rotors. The cross flow rotors have several advantages compared to the axial-flow rotors such as simpler in designing, easier to repair and they can rotate independently to the water direction. The popular rotors in the category of the cross flow rotors are Savonius rotor, Darrieus rotor and Gorlov rotor. Lately, Lucid developed cross flow spherical rotor to be installed within a pipeline to gather excess energy, which is available in the gravity-fed water pipelines [6]. In order to improve the efficiency of the cross flow rotors, the optimization of these systems is becoming necessary. In recent years, the number of studies interesting in the computational methods has been increased to study the cross flow rotors. In this context, with the use of CFD simulation, a numerical approach was developed by Satrio *et al.*, [7] to explore a Savonius water performance through the variation of the overlap distance and the aspect ratio. The rotor power coefficient increased at lower value of aspect ratio as a result of the increase in the rotor torque coefficient and at lower value of overlap distance due to the reduced pressure. The optimum rotor design was set with an aspect ratio of 0.61 and an overlap ratio of 0.1. It highlighted highest value of power coefficient of 0.48 at a current water velocity y of 0.9 m/s. Kumar and Saini [8] presented a numerical study of a Savonius water rotor with twisted blade profile having different values of twist angle ranging from 0° to 25° . In their work, they analyzed the hydrodynamic characteristics of the flow around the rotor such as the pressure, the velocity and the velocity streamlines. In addition, they noted that the twist angle and the Reynolds number had an effect on the performance of the Savonius water rotor. Payambarpour *et al.*, [9] investigated numerically a two-bladed Savonius water rotor with a deflector mounted upstream the flow. The impact of modifying the proposed deflector and the rotor geometrical parameters on the output torque and rotor efficiency as well as the flow rate was described across pressure contours and 3D streamlines. A positive effect of turbine height increment was recorded. The results showed that increasing turbine height had a good effect. However, increasing the deflector parameters was beneficial only up to a certain point, after which it had a negative impact on turbine performance. Using the Ansys Fluent 15.0, Kumar and Saini [10] studied a single stage modified Savonius water rotor with twisted blade profile. In their work, they analyzed the effect of the blade arc angle and the blade shape factor on the performance of the water rotor for different values of the tip speed ratio ranging from 0.5 to 1.0 and the water velocity ranging from $0.5 \text{ m}\cdot\text{s}^{-1}$ to $2 \text{ m}\cdot\text{s}^{-1}$. As a result, they noted that the optimal geometrical parameters for the modified Savonius water rotor with twisted blade profile are founded to be as blade arc angle of 150° and blade shape factor of 0.6. A numerical methodology was used by Patel and Patel [11] to examine the effect of applying variable load on a 60° twisted Savonius water turbine with an aspect ratio of 1 for the same flow rate. According to the numerical study, the greater the load on the shaft, the lower the power generated by the turbine, and conversely. Bachant and Wosnik [12] experienced a cylindrical Gorlov helical water rotor and a Lucid spherical water rotor. Results confirmed that the cylindrical Gorlov rotor outperformed the Lucid spherical rotor in terms of coefficient of power in a low-blockage tow tank or channel environment. Abdolahifar *et al.*, [13] studied the performance and the flow characteristics of a V-shaped blades Darrieus water rotor with two different blade shape twisted and non twisted with the use of 3D numerical simulations. Then they compared it with turbines

having straight and helical blades at top speed ratios from 0.69 to 1.5. The sweeping arrangement of the V-shaped and the helical shapes resulted in an inescapable span wise flow, thereby a performance loss, making neither type of V-shaped blade water rotor beneficial at low tip speed ratios. Talukdar *et al.*, [14] analyzed experimentally a Savonius water rotor based on the number of blades, the blade shapes and the immersion level. Also, they developed two-dimensional simulations for the design variants to analyze the flow characteristics and the aerodynamic performance of the turbines. The vertical-axis autorotation current turbine (VAACT) as a new form of vertical-axis water turbine was studied experimentally and numerically by Wu *et al.*, [15] with the aim of efficiency improvement through the shape improving. The numerical approach was based on response surface methodology (RSM) integrated into computational fluid dynamics (CFD) simulations. The optimal parameters gave a maximum power coefficient of 0.1545. This method, when compared to other optimization algorithms, significantly reduced the number of required sampling points. Derakhshan *et al.*, [16] analyzed experimentally and numerically a Hunter tidal turbine. As a result, they concluded that the power coefficient of a turbine increased for ducts with more area ratios. They noted also that in a four-turbine farm, the output power is maximum for a distance between neighbor turbines of 13D.

As mentioned above, researchers used computational methods to study the cross flow rotors performance. The choice of the numerical model parameters represents a sensitive and a required task to do. In this context, a variety of rotors were investigated mostly the Savonius and the Darrieus rotors. Indeed, with regard to the Lucid spherical water rotor, a nearer look at the literature review shows that it has not been fully explored despite its benefits. Thus, this paper relies on studying the numerical model parameters, namely the turbulence model, effect on the power coefficient and the hydrodynamic characteristics of the flow around a Lucid spherical rotor. The choice of the adequate turbulence model was based on the experimental results founded in anterior published studies.

2. Physical Models

Figure 1 shows the Lucid spherical rotor which is geometrically similar to the rotor developed by the Center for Ocean Renewable Energy (CORE) at the University of New Hampshire [12]. Bachant and Wosnik [12] studied experimentally a Lucid spherical water rotor which was manufactured by Lucid energy Technologies. The Lucid spherical rotor was tested in a test bed for vertical axis turbines. The total length of the test bed is equal to 36.6 m, the width is equal to 3.66 m and the depth is equal to 2.44 m. The rotor is made with four blades located around a center axis in equal intervals. It is characterized by a NACA 0020 airfoil with a chord equal to $c=140$ mm, a height equal to $H=0.97$ m, a diameter equal to $D=1.14$ m and a blade overlap equal to $e=2$.

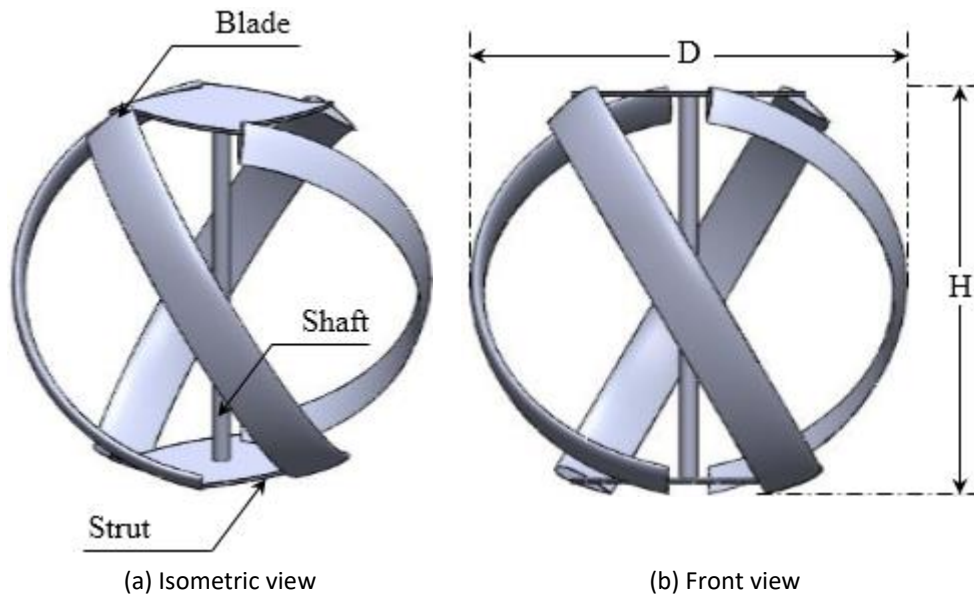


Fig. 1. Schematic of the Lucid spherical rotor

3. Computation Domains and Boundary Conditions

Three-dimensional numerical simulations of a Lucid spherical rotor were performed using Ansys Fluent 17.0. This commercial code solves the Navier-Stokes equations using a finite volume discretization method [17,18].

3.1 Table Style and Format

In order to use the sliding mesh technique, a fixed domain and a rotating domain separated by a sliding interface are created in Ansys “Design Modeler” as shown in Figure 2. The fixed domain has a length of $l=26$ m, a width of $w=3.66$ m and a height of $h=2.44$ m. The rotating domain, which encloses the Lucid spherical rotor, has a diameter of $d=1.2$ m. The inlet boundary condition has been set as the velocity of the water V_{∞} which is equal to $V_{\infty}=0.9$ m.s-1 on the left side of the fixed domain. The outlet boundary condition has been considered as a pressure outlet equal to the atmospheric pressure on the right side of the fixed domain. The left side and the right side of the fixed domain are taken at $l_1=10$ m and $l_2=16$ m from the rotation axis of the rotor, respectively. The rotation axis of the rotor is the z-axis. Slip boundary condition is assumed on the side and bottom walls of the fixed domain. Symmetry boundary is assigned to the top of the fixed domain. In addition, rotating wall with no-slip conditions has been set as boundary condition on the rotors’ blades. The rotational speed of the rotating region varies with the tip speed ratio and the water velocity. Therefore, a number of simulations are performed to obtain numerical results at the considered tip speed ratio. Which is calculated by the following equation:

$$\lambda = \frac{\omega R}{V_{\infty}} \quad (1)$$

where R is the radius of the rotor, ω is the rotational speed of the rotating domain and V_{∞} is the water speed.

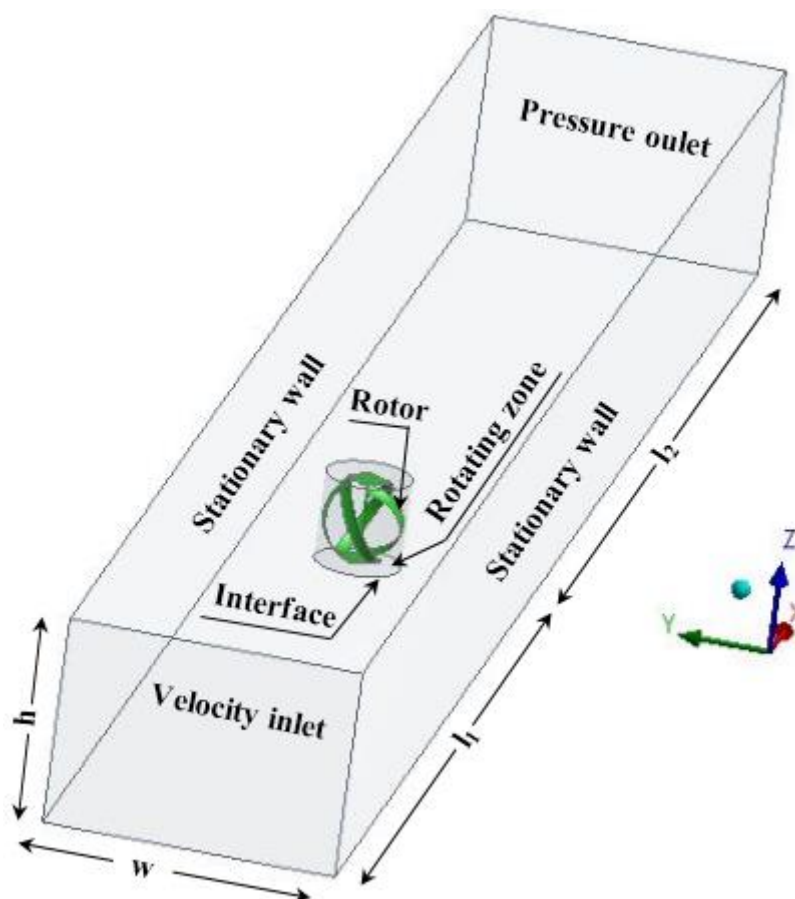


Fig. 2. Boundary conditions for CFD simulations

3.2 Meshing

In order to obtain accurate numerical results, the choice of the best meshing is needed. Indeed, a non-conformal unstructured mesh characterized by tetrahedral elements is adopted under the present study due to the complex rotor geometry. In this section, three meshing types have been studied in order to obtain mesh independent results. The choice of the appropriate meshing size is based on the comparison between our numerical results and the experimental results founded by Bachant and Wosnik [12]. The three meshing types are characterized by a number of elements ranging from 8.1 to 16 million. Fine mesh has been generated in the rotating domain compared to the mesh created in the fixed domain. In order to capture rapid changes of the hydrodynamic characteristics of the flow around the rotor, a prismatic mesh layer with inflation was created in the rotor blades, as shown in Figure 3. In order to calculate the distance of the first mesh node from the rotor blades surfaces, the y^+ value under the present study has been chosen less than one based on earlier studies. The rotor torque coefficient parameter C_m is chosen to be observed for the grid independence analysis. Numerical results are considered to be statistically stable, when the magnitude of torque coefficient fluctuations reaches quasi-steady state. Under the present study, simulations take four revolutions to attain the quasi-steady state. Figure 4 shows the effect of the mesh size on the rotor torque coefficient which was investigated for the last revolution. In fact, a meshing accuracy has been recorded for the second cost. In order to choose an accurate meshing size with a moderate time, the second mesh was chosen to minimize the calculation time of the resolution.

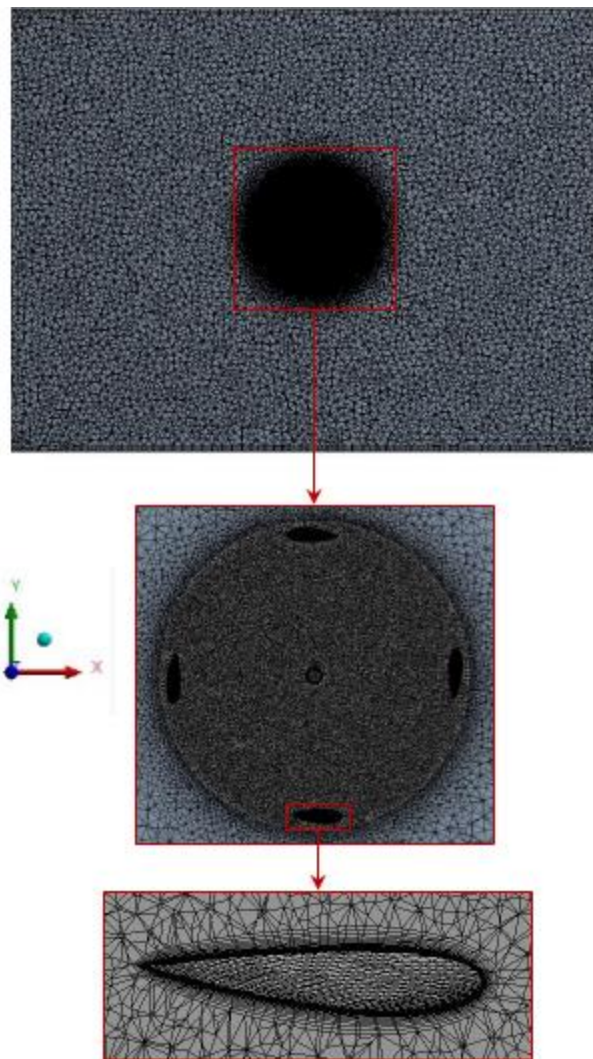


Fig. 3. Grids generation showing boundary layer near the rotor blades

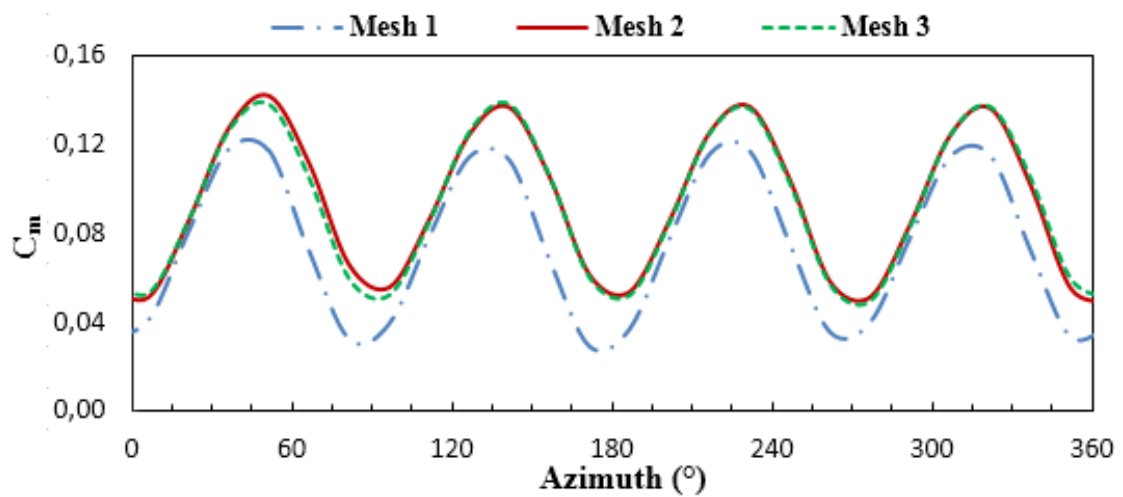


Fig. 4. Variation of the torque coefficient of the rotor at $\lambda=2.04$ respecting to the azimuth angle

3.3 Numerical Settings

Under the present study, the commercial computational fluid dynamics code Ansys Fluent 17.0 is used to solve the unsteady incompressible Reynolds-averaged Navier-Stokes equations. The governing equations are the Navier-Stokes equations [19-22]. The continuity equation is expressed in the following form:

$$\frac{\partial \rho}{\partial t} + \frac{\partial(\rho u_i)}{\partial x_i} = 0 \quad (2)$$

The momentum equations can be written as follows:

$$\frac{\partial(\rho u_i)}{\partial t} + \frac{\partial(\rho u_i u_j)}{\partial x_j} = -\frac{\partial p}{\partial x_i} + \frac{\partial}{\partial x_j} \left[\mu \left(\frac{\partial u_j}{\partial x_j} + \frac{\partial u_j}{\partial x_i} - \frac{2}{3} \delta_{ij} \frac{\partial u_i}{\partial x_i} \right) \right] + \frac{\partial(-\rho \overline{u_i u_j})}{\partial x_j} + F_i \quad (3)$$

where,

$$-\rho \overline{u_i u_j} = \mu_t \left(\frac{\partial u_i}{\partial x_j} + \frac{\partial u_j}{\partial x_i} \right) - \frac{2}{3} \rho k \delta_{ij} \quad (4)$$

The quantity $\overline{u_i u_j}$ is known as the turbulent stress, p is the pressure, ρ is the density of the water and F_i is a vector representing the external forces.

In order to solve the Navier-Stokes equations, a turbulence model is needed. Various turbulent models are available in Ansys Fluent.

The RNG k- ϵ model and the standard k- ϵ model present the same similar form and can be written as follows:

$$\frac{\partial}{\partial t}(\rho k) + \frac{\partial}{\partial x_i}(\rho k u_i) = \frac{\partial}{\partial x_j} \left(\alpha \mu_{\text{eff}} \frac{\partial k}{\partial x_j} \right) + G_k + G_b - \rho \epsilon - Y_M + S_k \quad (5)$$

$$\frac{\partial}{\partial t}(\rho \epsilon) + \frac{\partial}{\partial x_i}(\rho \epsilon u_i) = \frac{\partial}{\partial x_j} \left(\alpha_\epsilon \mu_{\text{eff}} \frac{\partial \epsilon}{\partial x_j} \right) + C_{1\epsilon} \frac{\epsilon}{k} (G_k + C_{3\epsilon} G_b) - C_{2\epsilon} \rho \frac{\epsilon^2}{k} - R_\epsilon + S_\epsilon \quad (6)$$

where G_k presents the generation of the turbulent kinetic energy due to the mean velocity gradients, G_b is the generation of the turbulent kinetic energy due to buoyancy, Y_M presents the contribution of the fluctuating dilatation in compressible turbulence to the overall dissipation rate, α_k and α_ϵ are respectively the inverse of the effective Prandtl numbers for k and ϵ . S_k and S_ϵ are the user-defined source terms. $C_{1\epsilon}$ and $C_{2\epsilon}$ are equal respectively to 1.42 and 1.68.

The modeled transport equations for k and ϵ in the realizable k- ϵ model are presented as follows:

$$\frac{\partial}{\partial t}(\rho k) + \frac{\partial}{\partial x_j}(\rho k u_j) = \frac{\partial}{\partial x_j} \left[\left(\mu + \frac{\mu_t}{\sigma_k} \right) \frac{\partial k}{\partial x_j} \right] + G_k + G_b - \rho \varepsilon - Y_M + S_k \quad (7)$$

$$\frac{\partial}{\partial t}(\rho \varepsilon) + \frac{\partial}{\partial x_j}(\rho \varepsilon u_j) = \frac{\partial}{\partial x_j} \left[\left(\mu + \frac{\mu_t}{\sigma_\varepsilon} \right) \frac{\partial \varepsilon}{\partial x_j} \right] + \rho C_1 S \varepsilon - \rho C_2 \frac{\varepsilon^2}{k + \sqrt{v \varepsilon}} + C_{1\varepsilon} \frac{\varepsilon}{k} C_{3\varepsilon} G_b + S_\varepsilon \quad (8)$$

where,

$$C_1 = \max \left[0.43, \frac{\eta}{\eta + 5} \right] \quad (9)$$

$$\eta = S \frac{k}{\varepsilon} \quad (10)$$

$$S = \sqrt{2 S_{ij} S_{ij}} \quad (11)$$

For the SST k- ω turbulence model, the transport equation for the turbulent kinetic energy k is given as follows:

$$\frac{\partial(\rho k)}{\partial t} + \frac{\partial}{\partial x_i}(\rho U_i k) = \frac{\partial}{\partial x_i} \left[\left(\mu + \frac{\mu_t}{\sigma_k} \right) \text{grad}(k) \right] + P_k - \beta^* \rho k \omega \quad (12)$$

Where:

$$P_k = \left(2\mu_t \frac{\partial U_i}{\partial x_j} \cdot \frac{\partial U_i}{\partial x_j} - \frac{2}{3} \rho k \frac{\partial U_i}{\partial x_j} \delta_{ij} \right) \quad (13)$$

σ_k and β^* are constants.

The transport equation for the turbulent frequency ω for the k- ω model is presented as follows:

$$\begin{aligned} \frac{\partial \rho \omega}{\partial t} + \frac{\partial}{\partial x_i}(\rho U_i \omega) = \\ \frac{\partial}{\partial x_i} \left[\left(\mu + \frac{\mu_t}{\sigma_{\omega,1}} \right) \text{grad}(\omega) \right] + \gamma_2 \left(2\rho \frac{\partial U_i}{\partial x_j} \cdot \frac{\partial U_i}{\partial x_j} - \frac{2}{3} \rho \omega \frac{\partial U_i}{\partial x_j} \delta_{ij} \right) - \beta_2 \rho \omega^2 + 2 \frac{\rho}{\sigma_{\omega,2} \omega} \frac{\partial k}{\partial x_k} \frac{\partial \omega}{\partial x_k} \end{aligned} \quad (14)$$

where β^* , β_2 , σ_k , $\sigma_{\omega,1}$, $\sigma_{\omega,2}$, γ_2 are constants and are equal respectively to 0.09, 0.083, 1, 2, 1.17, 0.44.

For the transition SST turbulence model, the transport equation for the intermittency γ is given as follows:

$$\frac{\partial(\rho\gamma)}{\partial t} + \frac{\partial(\rho U_{j\gamma})}{\partial x_j} = P_{\gamma 1} - E_{\gamma 1} + P_{\gamma 2} - E_{\gamma 2} + \frac{\partial}{\partial x_j} \left[\left(\mu + \frac{\mu_t}{\sigma_\gamma} \right) \frac{\partial \gamma}{\partial x_j} \right] \quad (15)$$

The transition sources are defined as follows:

$$P_{\gamma 1} = C_{a1} F_1 \rho S [\gamma F_o]^{C\gamma 3} \quad (16)$$

$$E_{\gamma 1} = C_{e1} P_{\gamma 1} \gamma \quad (17)$$

where S is the strain rate magnitude, F_1 is an empirical correlation that controls the length of the transition region and Ca_1 and Ce_1 hold the values of 2 and 1, respectively. The destruction/relaminarization sources are defined as follows:

$$P_{\gamma 2} = C_{a2} \rho \Omega \gamma F_t \quad (18)$$

$$E_{\gamma 2} = C_{e2} P_{\gamma 2} \gamma \quad (19)$$

where Ω is the vorticity magnitude. The transition onset is controlled by the following functions:

$$Re_v = \frac{\rho y^2 S}{\mu} \quad (20)$$

$$R_T = \frac{\rho k}{\mu \omega} \quad (21)$$

$$F_{o1} = \frac{Re_v}{2193 Re_{\theta c}} \quad (22)$$

$$F_{o2} = \min \left(\max \left(F_{o1}, F_{o1}^4 \right), 2.0 \right) \quad (23)$$

$$F_{o3} = \max \left(1 - \left(\frac{R_T}{2.5} \right)^3, 0 \right) \quad (24)$$

$$F_o = \max \left(F_{o2} - F_{o3}, 0 \right) \quad (25)$$

$$F_t = e^{-\left(\frac{R_T}{4} \right)^4} \quad (26)$$

where y is the wall distance and $Re_{\theta c}$ is the critical Reynolds number where the intermittency first starts to increase in the boundary layer. This occurs upstream of the transition Reynolds number

$\tilde{Re}_{\theta c}$ and the difference between the two must be obtained from an empirical correlation. Both the Fl and $Re_{\theta c}$ correlations are functions of $\tilde{Re}_{\theta c}$.

The constants for the intermittency equation are $C_{a1}=2$; $C_{e1}=1$; $C_{a2}=0.06$; $C_{e2}=50$; $C_{\gamma3}=0.5$ and $\sigma_{\gamma}=1.0$.

The transport equation for the transition momentum thickness Reynolds number $\tilde{Re}_{\theta t}$ is:

$$\frac{\partial(\rho \tilde{Re}_{\theta t})}{\partial t} + \frac{\partial(\rho U_j \tilde{Re}_{\theta t})}{\partial x_j} = P_{\theta t} + \frac{\partial}{\partial x_j} [\sigma_{\theta t} (\mu + \mu_t)] \frac{\partial \tilde{Re}_{\theta t}}{\partial x_j} \quad (27)$$

The source term is defined as follows:

$$P_{\theta t} = C_{\theta t} \frac{\rho}{t} (Re_{\theta t} - \tilde{Re}_{\theta t}) (1.0 - F_{\theta t}) \quad (28)$$

$$t = \frac{500\mu}{\rho U^2} \quad (29)$$

$$F_{\theta t} = \min \left(\max \left(F_w e^{\left(\frac{-y}{\delta}\right)^4}, 1.0 - \left(\frac{\gamma - 1/50}{1.0 - 1/50}\right)^2 \right), 1.0 \right) \quad (30)$$

$$\theta_{BL} = \frac{\tilde{Re}_{\theta t} \mu}{\rho U} \quad (31)$$

$$\delta_{BL} = \frac{15}{2} \theta_{BL} \quad (32)$$

$$\delta = \frac{50\Omega y}{U} \delta_{BL} \quad (33)$$

$$Re_{\omega} = \frac{\rho \omega y^2}{\mu} \quad (34)$$

$$F_w = e^{-\left(\frac{Re_{\omega}}{1E+5}\right)^2} \quad (35)$$

The model constants for the $\tilde{Re}_{\theta t}$ equation are $C_{\theta t}=0.03$ and $\sigma_{\theta t}=2.0$.

A simple pressure-velocity coupling method with second order upwind scheme for the convective terms is applied to realize simulations. The scaled residuals below 10^{-6} is considered as the convergence criteria for all residuals equations of continuity, momentum and turbulence

characteristics for each time step. The time step is defined as 1°/time step. Otherwise, the rotor turned 1° in each time step. The considered time step size is employed with 50 iterations per time step.

4. Comparison with Experimental Results

Figure 5 shows a comparison of the power coefficient between the numerical results and the experimental data established by Bachant and Wosnik [12] at range of tip speed ratios. The power coefficient is defined by the following equation:

$$C_p = \frac{P}{\frac{1}{2}\rho S V_\infty^3} = \lambda C_m \quad (36)$$

where P is the generated power and C_m is the rotor torque coefficient defined as follows:

The last parameter is given by the following equation:

$$S = 2RH \quad (37)$$

According to the obtained results, it can be observed that the realizable k-ε model and the transition SST turbulence model present a good agreement comparing numerical and experimental data. However, the maximum error of values is recorded for the RNG k-ε model and the SST k-ω model. Figure 6 shows the effect of the turbulence model on the rotor torque coefficient which was investigated for the last revolution at λ=2.04. Under the present study, simulations take four revolutions to attain the quasi-steady state of the magnitude of torque coefficient fluctuations.

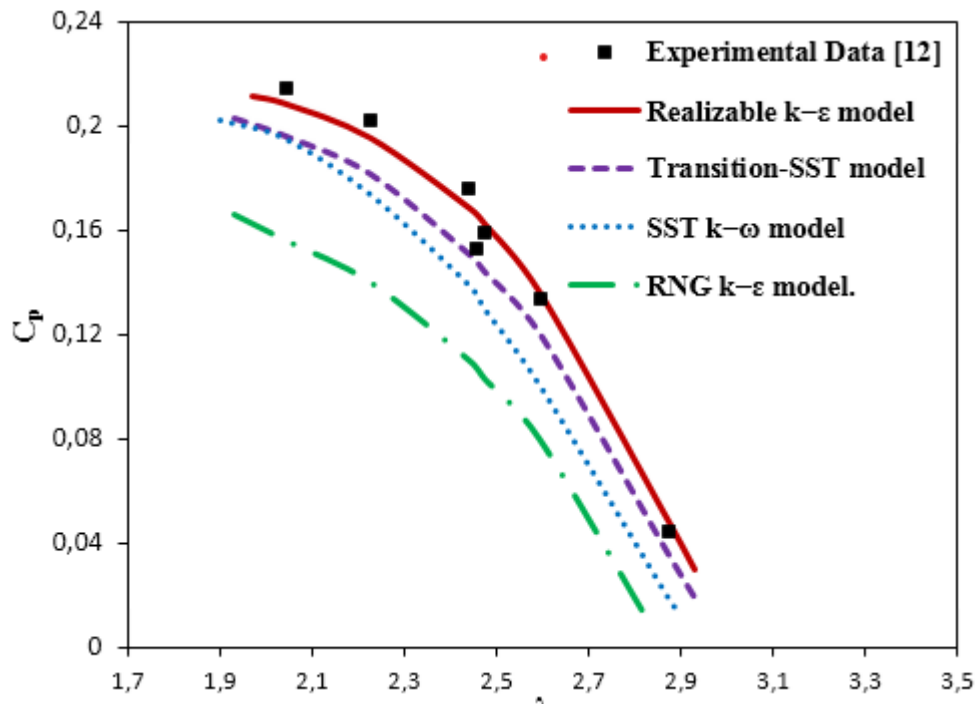


Fig. 5. Comparison with experimental results

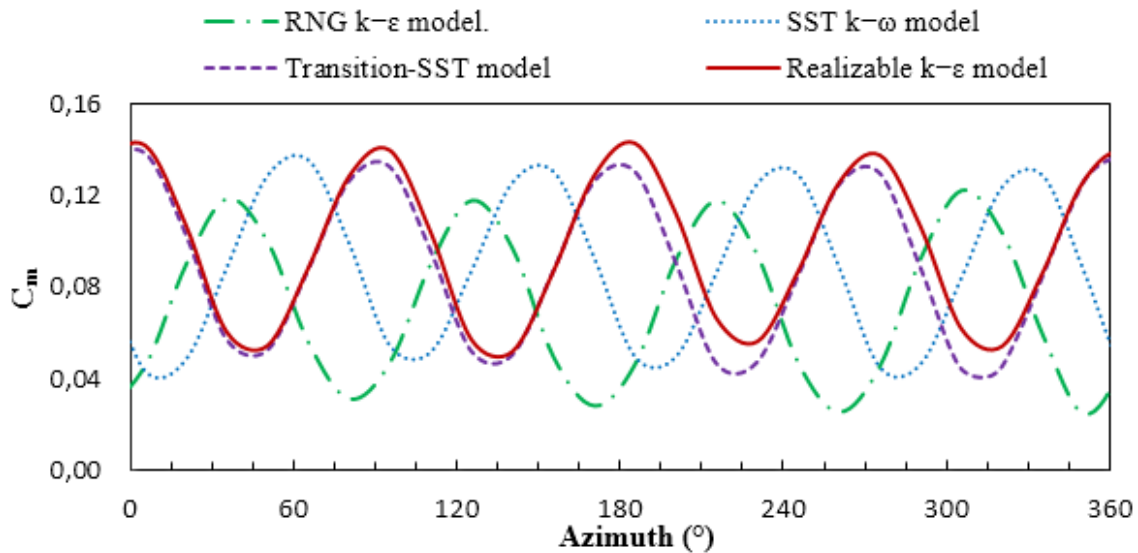


Fig. 6. Variation of the torque coefficient of the rotor at $\lambda=2.04$ respecting to the azimuth angle

5. Results and Discussion

The objective of this section is to study the hydrodynamic characteristics of the flow such as the magnitude velocity, the pressure, the turbulent kinetic energy, the dissipation rate of the turbulent kinetic energy and the turbulent viscosity distributions across the Lucid spherical rotor while varying the turbulence model. In these conditions, we are interested on the results presented in the visualization plane defined by $z=0$ m localized in the rotor mid-plane as presented in Figure 7.

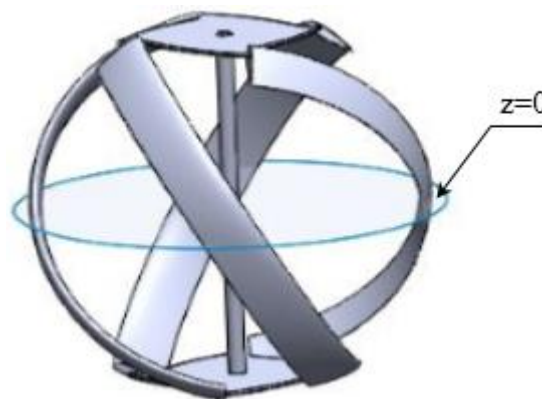


Fig. 7. Visualization plane

5.1 Magnitude Velocity

Figure 8 shows the distribution of the magnitude velocity of the water at $\lambda=2.04$ around the Lucid spherical rotor on the plane defined by $z=0$ m for the RNG k- ϵ model, the SST k- ω model, the transition SST model and the realizable k- ϵ model.

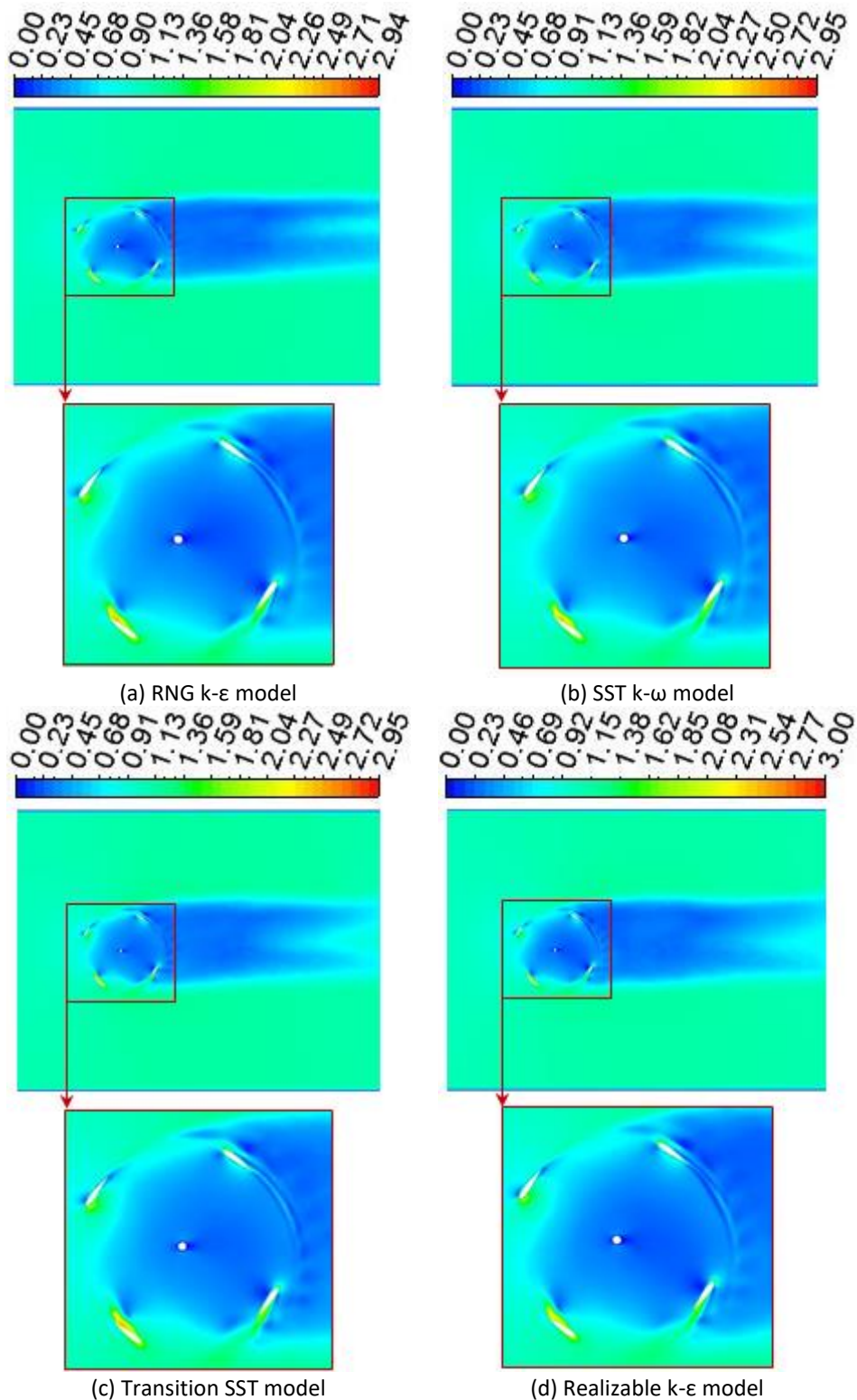


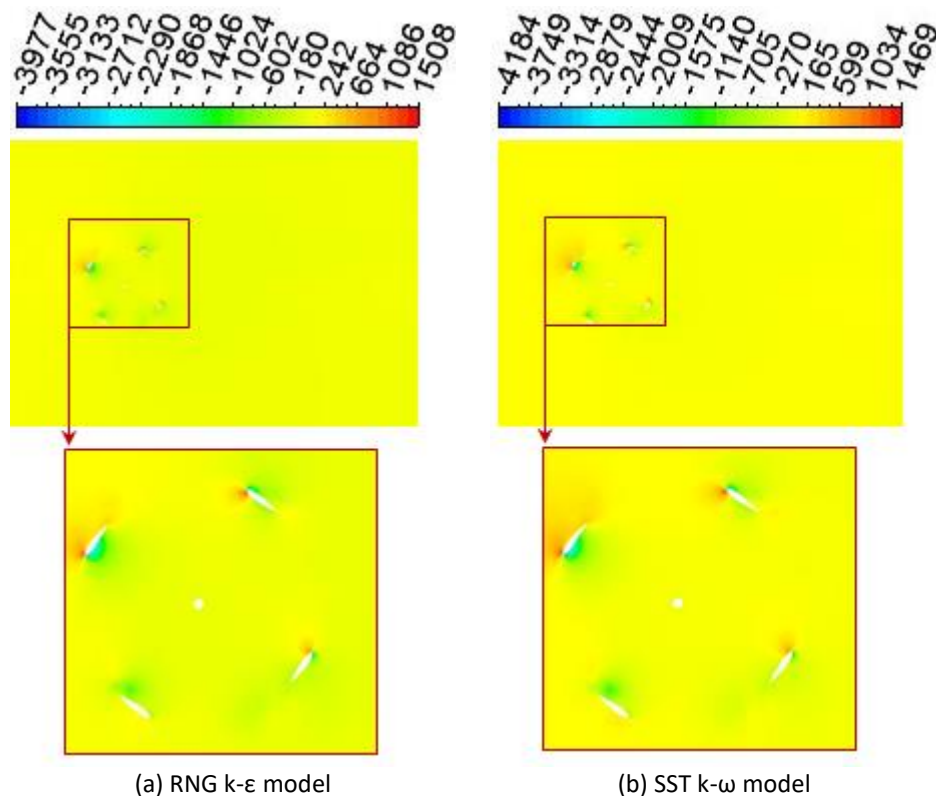
Fig. 8. Schematic of the Lucid spherical rotor

The comparison between these results shows that the used turbulence models present the same distributions. In fact, it can be noted that the velocity is weak in the upstream of the rotor and is equal to the value as given at the inlet boundary condition of the domain. The downstream of the rotor is characterized by a large deceleration zone which shows the trace of a low speed of the water. In addition, the large zone deflects upward slightly. This could be explained by the centrifugal force which is generated by the blades of the rotor with the counter-clockwise rotation.

While zooming the region surrounded the rotor, an acceleration zone of the flow is observed on the suction surface close to the leading edge. Therefore, a high-speed region on the suction side is appeared. While varying the turbulence model, a difference in values of the magnitude velocity has been noted. The maximum value of the magnitude water velocity is equal to $V=2.94 \text{ m.s}^{-1}$ using the RNG $k-\epsilon$ model, to $V=2.95 \text{ m.s}^{-1}$ using the SST $k-\omega$ model, to $V=2.95 \text{ m.s}^{-1}$ using the transition-SST model and to $V=3 \text{ m.s}^{-1}$ using the realizable $k-\epsilon$ model. Therefore, the comparison between these results confirms that the turbulence models affect the distribution of the magnitude velocity of the water around the Lucid spherical rotor.

5.2 Pressure

Figure 9 presents the pressure distribution around the Lucid spherical rotor for the RNG $k-\epsilon$ model, the SST $k-\omega$ model, the transition SST model and the realizable $k-\epsilon$ model on the plane $z=0 \text{ m}$. From these results, it has been observed that the pressure is uniform at the domain inlet. High values of the pressure are noticed at the upstream of the advancing blade, whereas low values are found at the downstream, which caused a difference of pressure. Energy is produced at this zone due to this difference of pressure. The comparison between these results showed that the turbulence model has a direct effect on the pressure distribution of the water around the Lucid spherical rotor. For example, the maximum value of the water pressure is equal to $p=1508 \text{ Pa}$ using the RNG $k-\epsilon$ model, to $p=1469 \text{ Pa}$ using the SST $k-\omega$ model, to $p=1570 \text{ Pa}$ using the transition-SST model and to $p=1507 \text{ Pa}$ using the realizable $k-\epsilon$ model.



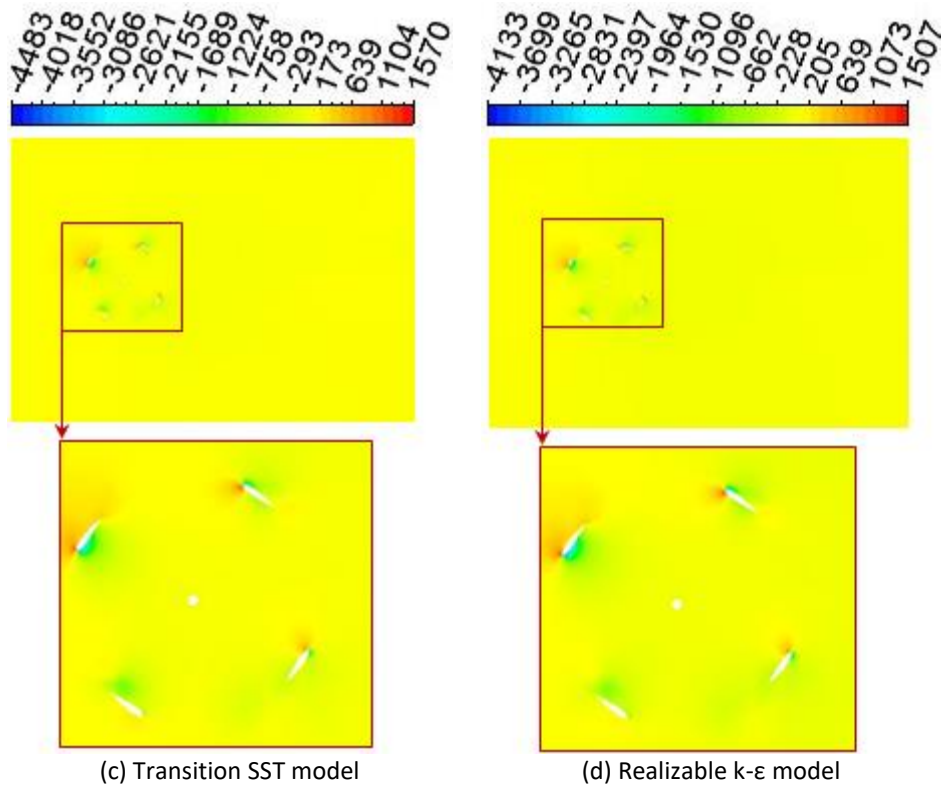
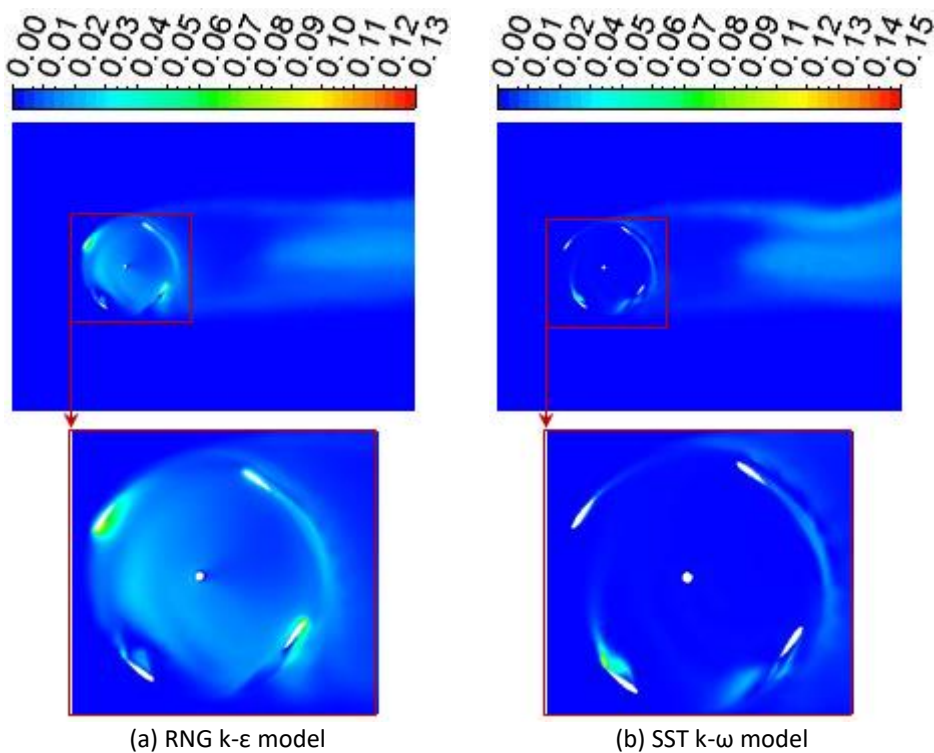


Fig. 9. Pressure distribution around the Lucid spherical rotor

5.3 Turbulent Kinetic Energy

Figure 10 shows the distribution of the turbulent kinetic energy at $\lambda=2.04$ around the Lucid spherical rotor for the RNG k- ϵ model, the SST k- ω model, the transition SST model and the realizable k- ϵ model on the plane defined by $z=0$ m.



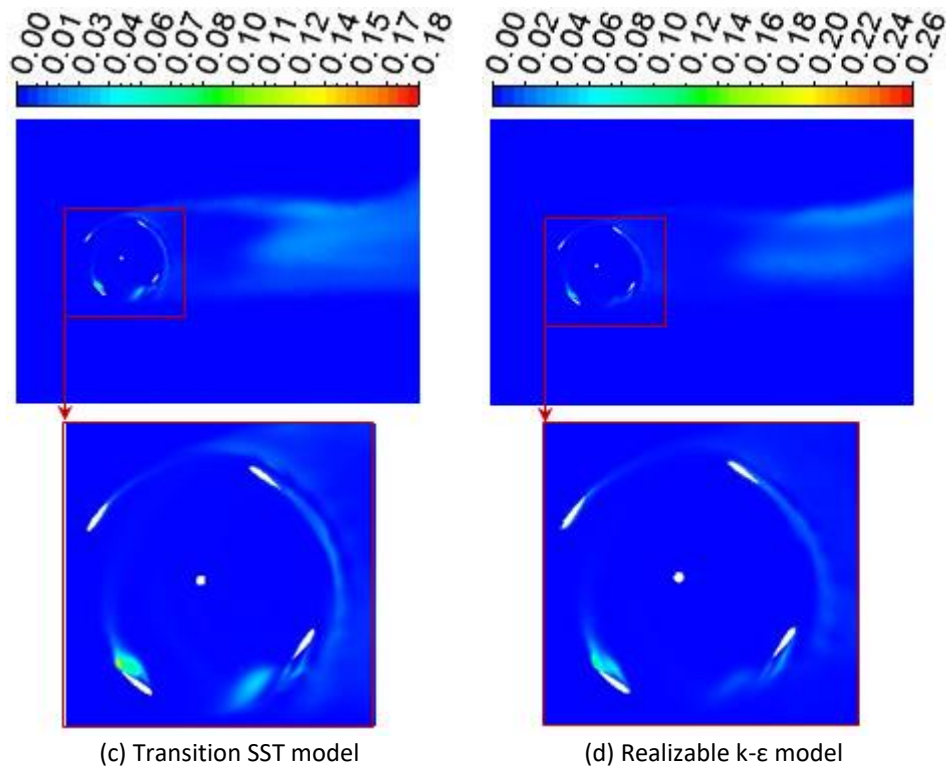


Fig. 10. Turbulent kinetic energy distribution around the Lucid spherical rotor

From these results, it is observed that the values of the turbulent kinetic energy are very low in the water channel except in the region surrounding the rotor. The turbulent kinetic energy distribution shows the increase of the energy near the rotor blades for the different considered cases. The comparison between these results confirms that the turbulent kinetic energy depends on the turbulence model. For example, the maximum value of the turbulent kinetic energy is equal to $k=0.13 \text{ m}^2 \cdot \text{s}^{-2}$ using the RNG $k-\epsilon$ model, to $k=0.15 \text{ m}^2 \cdot \text{s}^{-2}$ using the SST $k-\omega$ model, to $k=0.18 \text{ m}^2 \cdot \text{s}^{-2}$ using the transition-SST model and to $k=0.26 \text{ m}^2 \cdot \text{s}^{-2}$ using the realizable $k-\epsilon$ model.

5.4 Dissipation Rate of The Turbulent Kinetic Energy

Figure 11 shows the dissipation rate of the turbulent kinetic energy distribution around the Lucid spherical rotor on the plane $z=0 \text{ m}$ for the RNG $k-\epsilon$ model, the SST $k-\omega$ model, the transition SST model and the realizable $k-\epsilon$ model. From these results, it has been noted that a variation of the turbulence model has a direct effect on the distribution of the dissipation rate of the turbulent kinetic energy. From one case to another, it has been noted that the dissipation rate of the turbulent kinetic energy is weak at the upstream of the rotor. However, an increase of the dissipation rate of the turbulent kinetic energy is noticed near the blades of the rotor and at the downstream of the rotor. A difference in values of the dissipation rate of the turbulent kinetic energy has been noted while varying the turbulence model. In fact, the maximum value of the dissipation rate of the turbulent kinetic energy around the Lucid spherical rotor is equal to $\epsilon=0.23 \text{ m}^2 \cdot \text{s}^{-3}$ using the RNG $k-\epsilon$ model, to $\epsilon=0.47 \text{ m}^2 \cdot \text{s}^{-3}$ using the SST $k-\omega$ model, to $\epsilon=0.52 \text{ m}^2 \cdot \text{s}^{-3}$ using the transition-SST model and to $\epsilon=0.83 \text{ m}^2 \cdot \text{s}^{-3}$ using the realizable $k-\epsilon$ model.

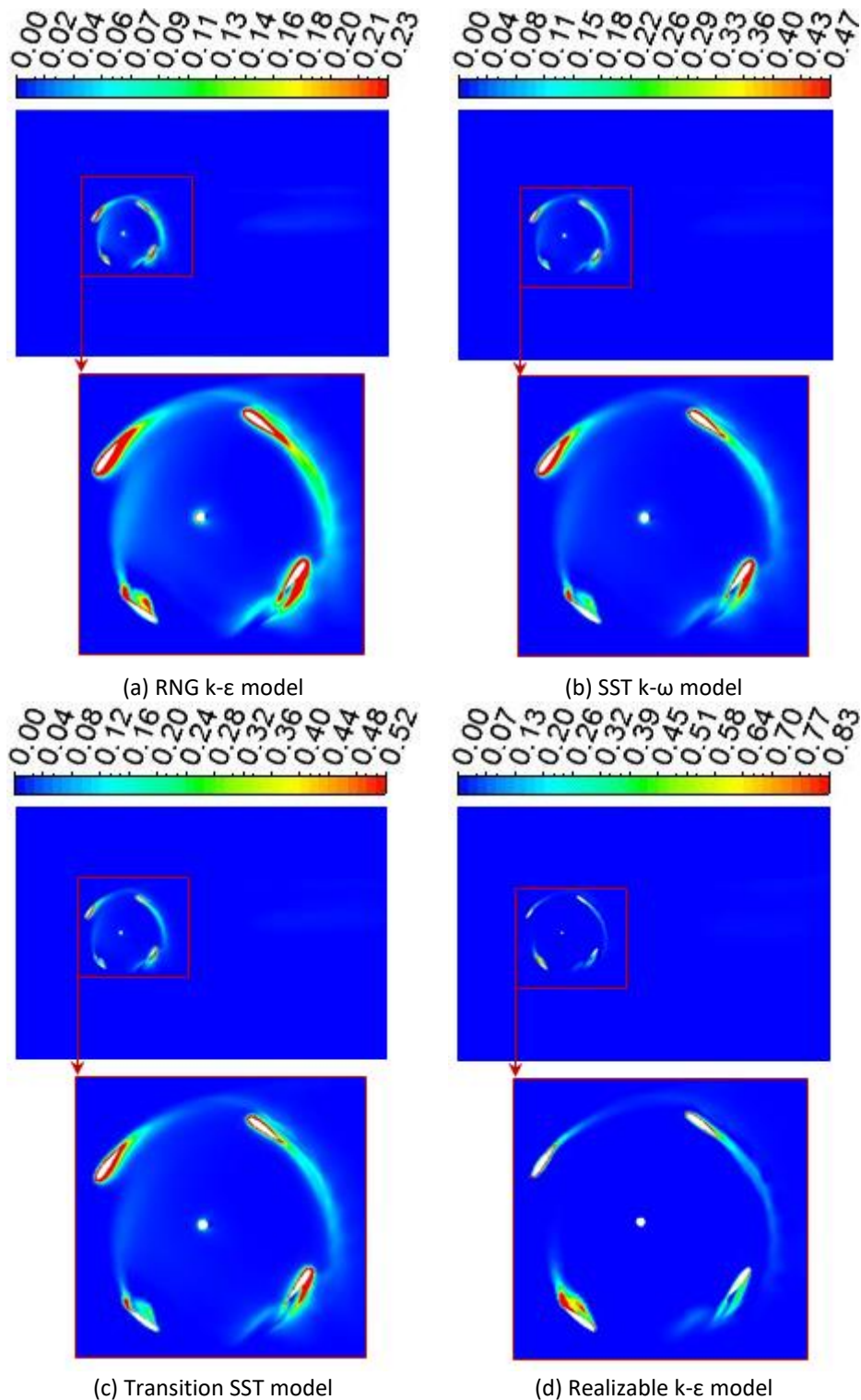


Fig. 11. Dissipation rate of the turbulent kinetic energy distribution around the Lucid spherical rotor

5.5 Turbulent Viscosity

Figure 12 shows the distribution of the turbulent viscosity for the RNG k- ϵ model, the SST k- ω model, the transition SST model and the realizable k- ϵ model at $\lambda=2.04$ around the Lucid spherical rotor on the plane defined by $z=0$ m.

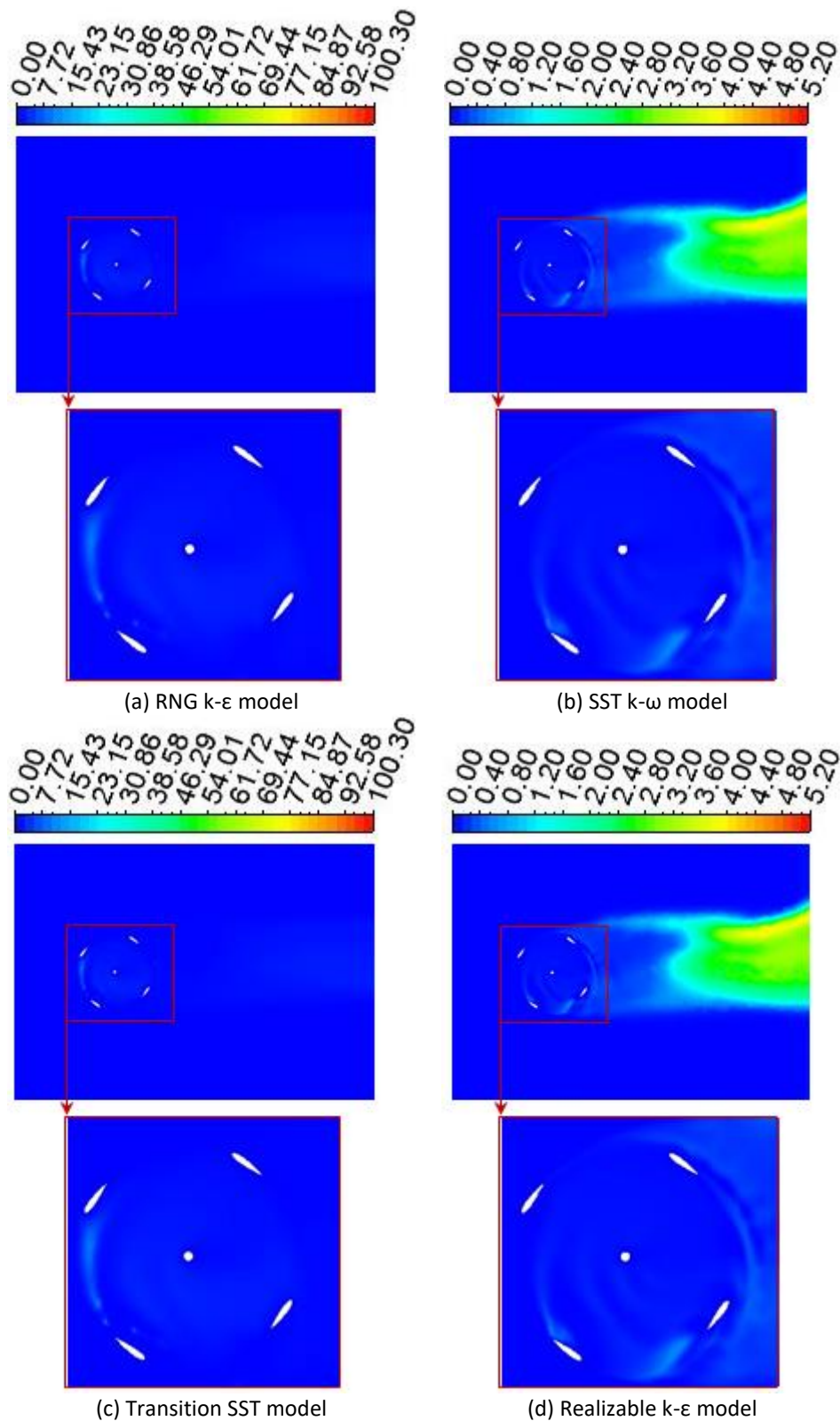


Fig. 12. Turbulent viscosity distribution around the Lucid spherical rotor

From these results, it is observed that the values of the turbulent kinetic energy are very low in the water channel except in the region surrounding the rotor. The turbulent kinetic energy distribution shows the increase of the energy near the rotor blades for the different considered cases. The comparison between these results confirms that the turbulent kinetic energy depends

on the turbulence model. For example, the maximum value of the turbulent kinetic energy is equal to $k=0.13 \text{ m}^2 \cdot \text{s}^{-2}$ using the RNG $k-\epsilon$ model, to $k=0.15 \text{ m}^2 \cdot \text{s}^{-2}$ using the SST $k-\omega$ model, to $k=0.18 \text{ m}^2 \cdot \text{s}^{-2}$ using the transition-SST model and to $k=0.26 \text{ m}^2 \cdot \text{s}^{-2}$ using the realizable $k-\epsilon$ model.

6. Conclusions

In this paper, numerical simulations were carried out to study the effect of the turbulence model on the numerical results. Practically, the RNG $k-\epsilon$ model, the SST $k-\omega$ model, the transition SST model and the realizable $k-\epsilon$ model were tested. The numerical simulations were based on the commercial unsteady Reynolds-Averaged Navier-Stokes (URANS) solver. The validation of the numerical method was performed using previous experiments founded at the literature. Numerical results showed that the turbulence models have a direct effect on the computational results. Indeed, the effect of the turbulence models on the hydrodynamic characteristics of the flow around the Lucid spherical rotor has been presented. For our future computational simulations, the realizable $k-\epsilon$ model is chosen to simulate the Lucid spherical rotor since it has shown a very good agreement with the experimental results.

Acknowledgement

The authors would like to thank the Laboratory of Electro Mechanic Systems (LASEM) members for the financial assistance.

References

- [1] Tezer, Tuba, Ramazan Yaman, and Gülşen Yaman. "Evaluation of approaches used for optimization of stand-alone hybrid renewable energy systems." *Renewable and Sustainable Energy Reviews* 73 (2017): 840-853. <https://doi.org/10.1016/j.rser.2017.01.118>
- [2] Guven, Gokhan, and Yusuf Sulun. "Pre-service teachers' knowledge and awareness about renewable energy." *Renewable and Sustainable Energy Reviews* 80 (2017): 663-668. <https://doi.org/10.1016/j.rser.2017.05.286>
- [3] Bakar, Nurul Asyikin Abu, Nujjiya A. Mu'in, and Noorfazreena M. Kamaruddin. "Design and Development of Savonius Turbine for STEM Education." *Journal of Advanced Research in Applied Sciences and Engineering Technology* 28, no. 2 (2022): 334-347. <https://doi.org/10.37934/araset.28.2.334347>
- [4] Shamsuddin, Muhd Syukri Mohd, and Noorfazreena Kamaruddin. "Experimental Investigation of the Power Storage System for Savonius Turbines in Wind and Water." *Journal of Advanced Research in Applied Sciences and Engineering Technology* 28, no. 3 (2022): 235-247. <https://doi.org/10.37934/araset.28.3.235247>
- [5] Bakar, Nurul Asyikin Abu, Muhd Syukri Mohd Shamsuddin, and Noorfazreena M. Kamaruddin. "Experimental Study of a Hybrid Turbine for Hydrokinetic Applications on Small Rivers in Malaysia." *Journal of Advanced Research in Applied Sciences and Engineering Technology* 28, no. 2 (2022): 318-324. <https://doi.org/10.37934/araset.28.2.318324>
- [6] Lahamornchaiyakul, Werayoot, and Nat Kasayapanand. "Free-Spinning numerical simulation of a novel vertical axis small water turbine generator for installation in a water pipeline." *CFD Letters* 15, no. 8 (2023): 31-49. <https://doi.org/10.37934/cfdl.15.8.3149>
- [7] Satrio, Dendy, Firdaus Yusri Muhammad, Mukhtasor, Shade Rahmawati, Sony Junianto, and Siti Musabikha. "Numerical simulation of cross-flow Savonius turbine for locations with low current velocity in Indonesia." *Journal of the Brazilian Society of Mechanical Sciences and Engineering* 44, no. 8 (2022): 315. <https://doi.org/10.1007/s40430-022-03620-w>
- [8] Kumar, Anuj, and R. P. Saini. "Performance analysis of a Savonius hydrokinetic turbine having twisted blades." *Renewable Energy* 108 (2017): 502-522. <https://doi.org/10.1016/j.renene.2017.03.006>
- [9] Payambarpour, S. Abdolkarim, Amir F. Najafi, and Franco Magagnato. "Investigation of deflector geometry and turbine aspect ratio effect on 3D modified in-pipe hydro Savonius turbine: Parametric study." *Renewable Energy* 148 (2020): 44-59. <https://doi.org/10.1016/j.renene.2019.12.002>
- [10] Kumar, Anuj, and R. P. Saini. "Performance analysis of a single stage modified Savonius hydrokinetic turbine having twisted blades." *Renewable Energy* 113 (2017): 461-478. <https://doi.org/10.1016/j.renene.2017.06.020>

- [11] Patel, Vimal, and Chirag Patel. "Performance investigation of twisted blade inline Savonius turbine at variable load condition using numerical method." *Materials Today: Proceedings* 49 (2022): 250-256. <https://doi.org/10.1016/j.matpr.2021.01.868>
- [12] Bachant, Peter, and Martin Wosnik. "Performance measurements of cylindrical-and spherical-helical cross-flow marine hydrokinetic turbines, with estimates of exergy efficiency." *Renewable Energy* 74 (2015): 318-325. <https://doi.org/10.1016/j.renene.2014.07.049>
- [13] Abdolahifar, Abolfazl, Mahdi Azizi, and Amir Zanj. "Flow structure and performance analysis of Darrieus vertical axis turbines with swept blades: A critical case study on V-shaped blades." *Ocean Engineering* 280 (2023): 114857. <https://doi.org/10.1016/j.oceaneng.2023.114857>
- [14] Talukdar, Parag K., Arif Sardar, Vinayak Kulkarni, and Ujjwal K. Saha. "Parametric analysis of model Savonius hydrokinetic turbines through experimental and computational investigations." *Energy Conversion and Management* 158 (2018): 36-49. <https://doi.org/10.1016/j.enconman.2017.12.011>
- [15] Wu, Hao, Antonio Carlos Fernandes, Renjing Cao, and Enhao Wang. "Performance evaluation and shape improvement of a novel vertical-axis autorotation current turbine." *Ocean Engineering* 284 (2023): 115086. <https://doi.org/10.1016/j.oceaneng.2023.115086>
- [16] Derakhshan, Shahram, Mohammadreza Ashoori, and Amirhosein Salemi. "Experimental and numerical study of a vertical axis tidal turbine performance." *Ocean Engineering* 137 (2017): 59-67. <https://doi.org/10.1016/j.oceaneng.2017.03.047>
- [17] Didane, Djamal Hissein, Muhammad Nur Arham Bajuri, Mahamat Issa Boukhari, and Bukhari Manshoor. "Performance Investigation of Vertical Axis Wind Turbine with Savonius Rotor using Computational Fluid Dynamics (CFD)." *CFD Letters* 14, no. 8 (2022): 116-124. <https://doi.org/10.37934/cfdl.14.8.116124>
- [18] Del Rio, Jorge Andrés Sierra, Alejandro Ruiz Sánchez, Daniel Sanín Villa, and Edwin Correa Quintana. "Numerical Study of H-Darrieus Turbine as a Rotor for Gravitational Vortex Turbine." *CFD Letters* 14, no. 8 (2022): 1-11. <https://doi.org/10.37934/cfdl.14.8.111>
- [19] Ayadi, Ahmed, Haithem Nasraoui, Abdallah Bouabidi, Zied Driss, Moubarak Bsis, and Mohamed Salah Abid. "Effect of the turbulence model on the simulation of the air flow in a solar chimney." *International Journal of Thermal Sciences* 130 (2018): 423-434. <https://doi.org/10.1016/j.ijthermalsci.2018.04.038>
- [20] Lajnef, Mariem, Mabrouk Mosbahi, Youssef Chouaibi, and Zied Driss. "Performance improvement in a helical Savonius wind rotor." *Arabian Journal for Science and Engineering* 45 (2020): 9305-9323. <https://doi.org/10.1007/s13369-020-04770-6>
- [21] Mosbahi, Mabrouk, Mariem Lajnef, Mouna Derbel, Bouzid Mosbahi, Costanza Aricò, Marco Sinagra, and Zied Driss. "Performance improvement of a drag hydrokinetic turbine." *Water* 13, no. 3 (2021): 273. <https://doi.org/10.3390/w13030273>
- [22] Mosbahi, Mabrouk, Mouna Derbel, Mariem Lajnef, Bouzid Mosbahi, Zied Driss, Costanza Aricò, and Tullio Tucciarelli. "Performance study of twisted Darrieus hydrokinetic turbine with novel blade design." *Journal of Energy Resources Technology* 143, no. 9 (2021): 091302. <https://doi.org/10.1115/1.4051483>